IDE: Image Dehazing and Exposure Using an Enhanced Atmospheric Scattering Model

Mingye Ju, Can Ding, *Member, IEEE,* Wenqi Ren, *Member, IEEE,* Yi Yang, Dengyin Zhang, *Member, IEEE,* and Y. Jay Guo, *Fellow, IEEE*

***Abstract*—Atmospheric scattering model (ASM) is one of the most widely used model to describe the imaging processing of hazy images. However, we found that ASM has an intrinsic limitation which leads to a dim effect in the recovered results. In this paper, by introducing a new parameter, i.e., light absorption coefficient, into ASM, an enhanced ASM (EASM) is attained, which can address the dim effect and better model outdoor hazy scenes. Relying on this EASM, a simple yet effective gray-world-assumption-based technique called IDE is then developed to enhance the visibility of hazy images. Experimental results show that IDE eliminates the dim effect and exhibits excellent dehazing performance. It is worth mentioning that IDE does not require any training process or extra information related to scene depth, which makes it very fast and robust. Moreover, the global stretch strategy used in IDE can effectively avoid some undesirable effects in recovery results, e.g., over-enhancement, over-saturation, and mist residue, etc. Comparison between the proposed IDE and other state-of-the-art techniques reveals the superiority of IDE in terms of both dehazing quality and efficiency over all the comparable techniques.**

***Index Terms*—Haze removal, Gray world assumption, Atmospheric scattering model, Illumination compensation, Scene exposure.**

I. Introduction

HAZE is a common natural phenomenon in the real world that severely lowers contrast and shifts the inherent colour of an image, particularly for outdoor scenes captured in inclement weather. These low-contrast images taken in hazy conditions usually do not contain sufficient information to guarantee the proper operation of vision systems [1], [2]. Therefore, robust and efficient image haze removal technology is crucial for removing adverse effects and reconstructing blurred information.

The most intuitive way of restoring the hazy image is to locally or globally increase its contrast by traditional enhancement methods [3]–[7]. However, these methods ignore the physical degradation process of hazy images, thus the visual quality of recovered results is limited. To compensate for this deficiency, fusion-wise visibility enhancement techniques were proposed [8]–[10]. In these works, by utilizing two or more traditional methods, hazy input images are first transformed into several enhanced images with different attributes. Then, according to haze-related features, these enhanced images are blended to a highly dynamic result using Laplacian pyramid representation. Another kind of solution advocated in [11]–[14] is based on atmospheric scattering model (ASM) [11], and they generate high-quality results by making full use of additional information. Regrettably, these approaches require extra and high-cost premises, thereby limiting their practicability in many applications [15], [16]. Typically, in [12], geo-reference terrains and urban models are needed to realize haze removal for contaminated images. However, terrain or models are difficult to obtain in most scenarios.

During the past few decades, we have witnessed a significant progress in single image haze removal. In general, currently available methods can be categorized into two groups: prior-based techniques and learning-based techniques.

Prior-Based Techniques: The core idea of these methods [17]–[30] is to utilize the potential prior knowledge to decrease the uncertainty of scene depth to estimate the imaging parameters and then restore the haze-free result via ASM. For example, dark channel prior (DCP) was proposed in [17] to detect the haze distribution of hazy images. Given the haze distribution, realistic haze-free results can be attained by refining the initial transmission. In [18], haze removal was implemented according to a key observation that a linear relationship exists in the minimum channel between hazy image and scene albedo. Relying on haze-lines prior, Berman et al. [19], [20] formulated the dehazing task into an energy minimization problem. In [21], gamma correction prior (GCP) was proposed to synthesize a virtual transformation of hazy images, and global dehazing was later designed by extracting the scene depth from this transformation and hazy image. To achieve the balance of luminance and contrast, Liu et al. [22] reformulated the haze removal problem into a luminance reconstruction scheme. Similarly, Bui et al. [23] developed a colour-ellipsoid-prior-based image dehazing technology by jointly considering the contrast and the over-saturation. Ju et al. [24] presented a Bayesian method to perform haze removal for single images by fusing the multiple image priors. In [25], a super-pixel-based strategy was designed to realize haze removal for hazy images.

Manuscript submitted 2020. This work was supported by National Natural Science Foundation of China (61902198, 61872423) and Natural Science Foundation of Jiangsu Province (BK20190730), and Research Fund of Nanjing University of Posts and Telecommunications (NY219135). (*Corresponding authors: Can Ding and Wenqi Ren)*

M. Ju and D. Zhang are with the School of Internet of Things, Nanjing University of Posts and Telecommunications, Nanjing, 210000, China. e-mail:(Jumingye@njupt.edu.cn, zhangdy@njupt.edu.cn)

C. Ding and Y. Jay Guo are with the Global Big Data Technologies Centre (GBDTC), University of Technology Sydney (UTS), Ultimo, NSW, 2007, Australia. e-mail:(Can.Ding@uts.edu.au, Jay.Guo@uts.edu.au)

Y. Yang is with the Centre for Artificial Intelligence (CAI), University of Technology Sydney (UTS), Ultimo, NSW, 2007, Australia. e-mail:(Yi.Yang@uts.edu.au)

W. Ren is with the State Key Laboratory of Information Security, Institute of Information Engineering, Chinese Academy of Sciences, Beijing, 100000, China. e-mail:(renwenqi@iie.ac.cn)

Learning-Based Techniques: According to colour attenuation prior (CAP), Zhu et al. [31] constructed a linear model on scene depth and then determined the parameters in this model with a supervised regression, thereby restoring a haze-free result from single input image. Unlike [31], subsequent learning-based approaches [32]–[42] realized haze removal by self-learning or merging the haze-relevant features using machine learning. For instance, inspired by the well-known image priors, a convolutional neural network (CNN)-based system called DehazeNet [32] was proposed to attain an end-to-end image dehazing. In [33], a multiscale CNN (MSCNN) was established to improve the recovery performance by learning more features. In subsequence, an All-in-One Dehazing Network (AoD-Net) [34] was devised by formulating the ASM, which can reduce the errors accumulated in the parameter estimation. To better deal with real-world hazy images, a DCP loss-based unsupervised dehazing architecture [35] was trained via real-world outdoor samples. In [36], an advanced dehazing network containing two parts, i.e., perception-inspired dehazing and refinement subnetworks, was created. Similar to [8]–[10], Ren et al. developed a gated fusion network [37] by fusing three inputs preprocessed from hazy images. To achieve more effective features, a ranking-CNN network [38] was proposed by extending the structure of CNN to ensure that the statistical and structural attributes of hazy images can be simultaneously captured. In [39], a generative adversarial network called HRGAN consisting of a generator network and a discriminator network was proposed to achieve visual haze removal. In [40], a trainable CNN named GridDehazeNet, consisting of preprocessing, backbone, and postprocessing modules, was proposed for single image dehazing. To restore the binocular hazy image pairs, a binocular image dehazing Network (BidNet) was developed by Pang et al. in [41], which can explore the correlations between the binocular image pairs to improve the recovery quality. For better dehazing performance on real-world images, Shao et al. [42] devised a domain adaptation framework which contains a translation module and two dehazing modules.

Although aforementioned techniques can rule out haze cover in hazy images to some extent, they lack the capability to clearly reveal the details and textures for dehazed scenes, especially for close-range scenes. There are currently two strategies used to address this dim effect problem. The first strategy [20] is to employ postprocessing operators to improve the global contrast. Its main advantage is high efficiency, but this operator may destroy the image structure and introduce colour cast in recovery results. Another strategy [24], [43], [44] is based on the observation of uneven illumination, which removes the dim effect by reforming the global atmospheric light in ASM as a matrix-form local illumination. However, the computational overhead is inevitably increased since the redefined ASM has a higher uncertainty than that of ASM.

In this paper, it is found that the observed dim effect is mainly because ASM fails to consider the light trapping phenomenon related to the texture density and scene depth. To compensate for this limitation, a new parameter, i.e., the light absorption coefficient, is introduced to improve ASM. The novel ASM with enhanced robustness (EASM) can address this dim effect and better model the imaging process of hazy scenes. Based on this EASM, a fast image processing technique called IDE is developed to realize dehazing and exposure for single hazy images. Specifically, the transcendental equation (TE) on transmission is first deduced by imposing the gray-world assumption on EASM. To reduce the computational complexity, the TE is then converted into an unary quadratic equation by replacing the logarithmic function in TE as a fitting rational function, which makes transmission directly solvable. Finally, global stretch strategy (GSS) is designed to search the only unknown constant, namely the minimum transmission value in the whole image, thereby restoring a high-quality haze-free result via EASM. As an example, the comparison between the proposed IDE and the well-known DCP [17] on two example images is illustrated in Fig. 1.

Fig. 1. Comparison between the well-known DCP and the proposed IDE on two example images. **Left**: Hazy Images. **Middle**: Results dehazed via DCP. **Right**: Results dehazed via IDE.

II. Enhanced Atmospheric Scattering Model (EASM)

A. Limitation of Atmospheric Scattering Model (ASM)

In computer vision and computer graphics, atmospheric scattering model (ASM) [11] is widely used to describe the degradation process of single hazy images. Mathematically, it is modelled as follows:

$$\boldsymbol{I}(x,y) = \boldsymbol{A} \cdot \boldsymbol{\rho}(x,y) \cdot t(x,y) + \boldsymbol{A} \cdot (1 - t(x,y)), \quad (1)$$

where $\boldsymbol{I}$ is the hazy image, $\boldsymbol{A}$ is atmospheric light assumed to be a constant, $\boldsymbol{\rho}$ is scene albedo (haze-free image), and t is medium transmission. When the distribution of particles suspended in the atmosphere is spatially homogeneous, the transmission t can be expressed as:

$$t(x,y) = e^{-\beta \cdot d(x,y)}, \quad (2)$$

where d and β are the scene depth and scattering coefficient, respectively. In ASM, the first term on the right side is used to describe the direct impact of scene reflection light caused by haze. This term is named as Direct Attenuation and decays exponentially with the scene depth d. The second term, called Airlight, increases with the scene depth d [21].

As mentioned in the introduction, ASM-based dehazing techniques can recover haze-free results for most single hazy

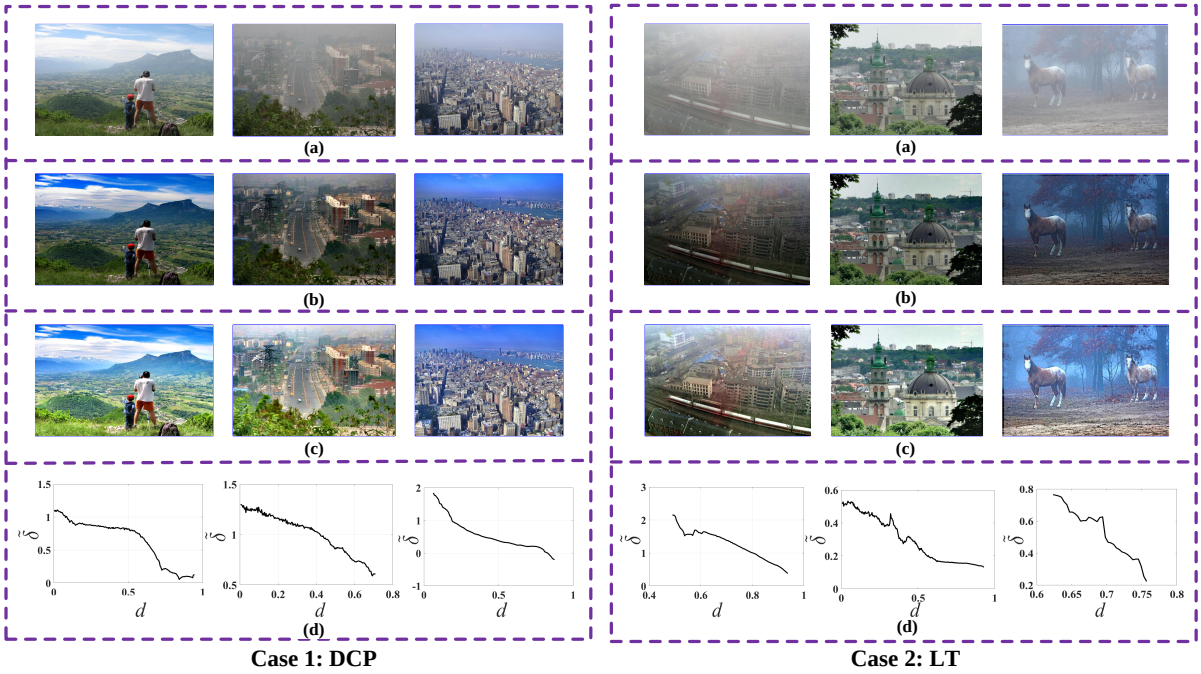

Fig. 2. Illustration of the dim effect caused by ASM using six different types of sample images collected from the real world. **First row**: Hazy images. **Second row**: Recovered scene albedo by DCP and LT. **Third row**: Recovered real scene albedo using Retinex. **Bottom row**: Variations of $\hat{\delta}$ with the scene depth d.

images, but the recovery scenes always appear to be too dim. In fact, although the incident atmospheric light is a constant, it has different illumination effects on different scenes, as the light can be trapped/absorbed in textures and the light absorption rate changes with the texture density. In [45], light trapping was achieved by introducing disordered nanotextures on graphene, which increased the light absorption rate at the micro level. Similarly, in the macro-view, we found that the light absorption rate is also larger with a higher texture density. Compared to long-range scenes in a haze-free image, short-range scenes have richer textures that exhibit a stronger absorption of light (the light becomes diffracted, scattered, and trapped in cavities). Assuming the light absorption coefficient is $\alpha \in (0, 1]$, then the reflected light is $(1 - \alpha) \cdot \boldsymbol{A} \cdot \boldsymbol{\rho}$, which has a lower intensity than the expected light in ASM, i.e., $\boldsymbol{A} \cdot \boldsymbol{\rho}$. Without considering the light absorption, the recovered scene albedo using ASM will be smaller than the real scene albedo, $\boldsymbol{\rho}_{ASM} < \boldsymbol{\rho}_{real}$; thus, the scenes will look darker. Moreover, the level of the dim effect changes with the scene depth due to the different light absorption rates at different scene depths.

To illustrate the drawback of ASM, six different types of hazy images were collected from the real world and dehazed by the ASM-based techniques, i.e., DCP [17] and LT [18]. The hazy images and the recovered scene albedos ($\boldsymbol{\rho}_{ASM}$) are shown in the first and second rows of Fig. 2. Subsequently, Retinex [46] was applied to the dehazed results to suppress the distortion caused by the uneven illumination in the images, thereby attaining the real scene albedos ($\boldsymbol{\rho}_{real}$) (the third row in Fig. 2). By comparing the second and third rows of Fig. 2, it can be observed that the recovered results using ASM-based dehazing techniques appear to be darker, especially for the short-range scenes. Moreover, to quantitatively demonstrate the relationship between the scene depth and the dim effect, we first determined the depth map via widely accepted CAP [31]. Then the relative error of the scene albedos modelled by ASM

$$\hat{\delta} = \frac{\boldsymbol{\rho}_{real} - \boldsymbol{\rho}_{ASM}}{\boldsymbol{\rho}_{ASM}} \tag{3}$$

was calculated. The variations in $\hat{\delta}$ with the scene depth d for each hazy input image are shown in the last row of Fig. 2. For all six sample images, the relative error $\hat{\delta}$ is monotonically decreasing with d in general. In other words, the dim effect caused by ASM becomes stronger with a smaller scene depth.

B. Enhanced ASM (EASM)

To eliminate this limitation of ASM, the light absorption coefficient $\alpha \in (0, 1]$ is introduced into ASM. The enhanced ASM can be expressed as

$$\boldsymbol{I}(x, y) = \boldsymbol{A} \cdot (1 - \alpha(x, y)) \cdot \boldsymbol{\rho}(x, y) \cdot t(x, y) + \boldsymbol{A} \cdot (1 - t(x, y)). \tag{4}$$

Note that the vast majority of particles suspended in the scattering path are still exposed under the sun [47]; thus, the atmospheric light in Airlight is maintained, i.e., the second term in Eq. 1 remains the same. As can be intuitively imagined and evidenced by the results shown in Fig. 2, as d decreases, the dim effect and the light absorption become stronger (α increases). Since α decreases with d and its maximum value should be 1, we define α as

$$\alpha(x, y) = 1 - \frac{d(x, y)}{\max(d)}. \tag{5}$$

From Eq. 2, we know that

$$d(x,y) = -\frac{ln(t(x,y))}{\beta}. \tag{6}$$

By substituting Eq. 6 into Eq. 5, the light absorption coefficient α can be rewritten as

$$\alpha(x,y) = 1 - \frac{\ln(t(x,y))}{\ln(t_{min})}, \tag{7}$$

where $t_{min} = e^{-\beta \cdot \max(d)}$ represents the minimum transmission value of an image. Then, substituting Eq. 7 into Eq. 4, the enhanced ASM (EASM) with exposure capability is obtained as

$$\boldsymbol{I}(x,y) = \boldsymbol{A} \cdot \frac{\ln(t(x,y))}{\ln(t_{min})} \cdot \boldsymbol{\rho}(x,y) \cdot t(x,y) + \boldsymbol{A} \cdot (1 - t(x,y)). \tag{8}$$

It should be pointed out that EASM does not loose the haze removal solution space since the newly introduced parameter $\boldsymbol{\alpha}$ is only related to transmission t. Nevertheless, because of the insufficient available information, EASM-based dehazing is still an ill-posed problem.

III. Image Dehazing Based on EASM (IDE)

In this section, based on gray-world assumption (GWA) [48] and EASM described in the previous section, a fast visibility recovery method called IDE is developed. It can simultaneously dehaze and expose single hazy images without any extra requirements. Only three modules are utilized in IDE, i.e., the priori constraint module, fast calculation module, and scene albedo recovery module.

A. Priori Constraint

GWA, which assumes the average albedos of three colour channels of a scene tend to be a same constant and are achromatic (gray) [48], has been successfully used for colour cast correction [49]–[51]. In this work, we make use of GWA to restrict the uncertainty of EASM by considering each local patch in an input image as a small scene. In specific, we first assume that the transmissions in a local patch are a constant and denote them as $\tilde{t}$. Then, the mean operation is performed on both sides of EASM (Eq. 8) for a local patch:

$$\hat{I}(x,y) = \hat{A} \cdot \frac{\ln(\tilde{t}(x,y))}{\ln(t_{min})} \cdot \hat{\rho}(x,y) \cdot \tilde{t}(x,y) + \hat{A} \cdot (1 - \tilde{t}(x,y)), \tag{9}$$

where $\hat{A}$ is the mean of atmospheric light of different colour channels and $\hat{I}$ and $\hat{\rho}$ are the local means of $\boldsymbol{I}$ and $\boldsymbol{\rho}$, respectively. Mathematically, they can be expressed by

$$\begin{cases} \hat{I}(x,y) = \frac{1}{3 \cdot |\Omega(x,y)|} \sum_{c \in \{R,G,B\}} \sum_{(x',y') \in \Omega(x,y)} I^c(x',y') \\ \hat{\rho}(x,y) = \frac{1}{3 \cdot |\Omega(x,y)|} \sum_{c \in \{R,G,B\}} \sum_{(x',y') \in \Omega(x,y)} \rho^c(x',y') \\ \hat{A} = \frac{1}{3} \cdot \sum_{c \in \{R,G,B\}} A^c, \end{cases} \tag{10}$$

where c is the colour channel index, $\Omega(x,y)$ is the local patch centered at coordinate (x,y), and I^c, ρ^c, and A^c are the hazy component, scene albedo, and atmospheric light in the i colour channel, respectively. According to GWA, the average albedo of a local patch (which is considered a small image in this work) can be approximated as

$$\hat{\rho}(x,y) = \frac{1}{2} \tag{11}$$

according to [9], [48]. Note that this is more accurate when the local patch size s is larger. When s is smaller, this approximation has a lower accuracy. The local patch size s was optimized to be 75×75 in this work. Details of the optimization are given in Section IV-A.

With this approximation, Eq. 9 is simplified as:

$$\hat{I}(x,y) = \hat{A} \cdot \frac{\ln(\tilde{t}(x,y))}{2 \cdot \ln(t_{min})} \cdot \tilde{t}(x,y) + \hat{A} \cdot (1 - \tilde{t}(x,y)). \tag{12}$$

This equation is a transcendental equation that is difficult to solve directly due to the contained logarithmic function. In the following subsection, an efficient fitting function is introduced to solve Eq. 12.

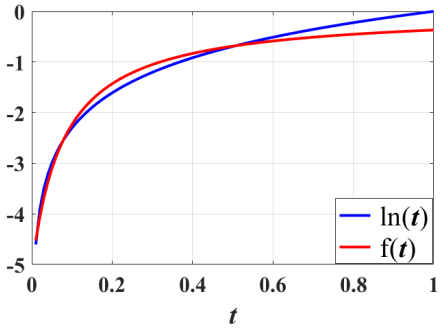

Fig. 3. The curves of the logarithmic function and the fitted rational function in Eq. 13.

B. Fast Calculation

To make Eq. 12 solvable, a rational function $f(\cdot)$ is utilized to replace the logarithmic function $\ln(\cdot)$ in the equation. The rational function is expressed as

$$\ln(\tilde{t}(x,y)) \approx f(\tilde{t}(x,y)) = \frac{p_1}{p_2 + \tilde{t}(x,y)}, \tag{13}$$

where $p_1 = -0.397$ and $p_2 = 0.07747$ were optimized to fit the logarithmic function using MATLAB cftool. The curves of the logarithmic function $\ln(t)$ and the rational function $f(t)$ used to fit $\ln(t)$ are compared in Fig. 3. According to the figure, the two functions agree quite well with each other.

Substituting Eq. 13 into Eq. 12, the transcendental equation is converted into

$$\left(\ln(t_{min}) \cdot (\hat{I}(x,y) + \hat{A} \cdot p_2 - \hat{A}) - \frac{1}{2} \cdot \hat{A} \cdot \ p_1\right) \cdot \tilde{t}(x,y) + \hat{A} \cdot \ln(t_{min}) \cdot \left(\tilde{t}(x,y)\right)^2 + p_2 \cdot \ln(t_{min}) \cdot \left(\hat{I}(x,y) - \hat{A}\right) = 0. \tag{14}$$

Note that this equation is an unary quadratic equation. For clarity, it is rewritten as

$$\lambda_1 \cdot \left(\hat{t}(x,y)\right)^2 + \lambda_2(x,y) \cdot \hat{t}(x,y) + \lambda_3(x,y) = 0, \tag{15}$$

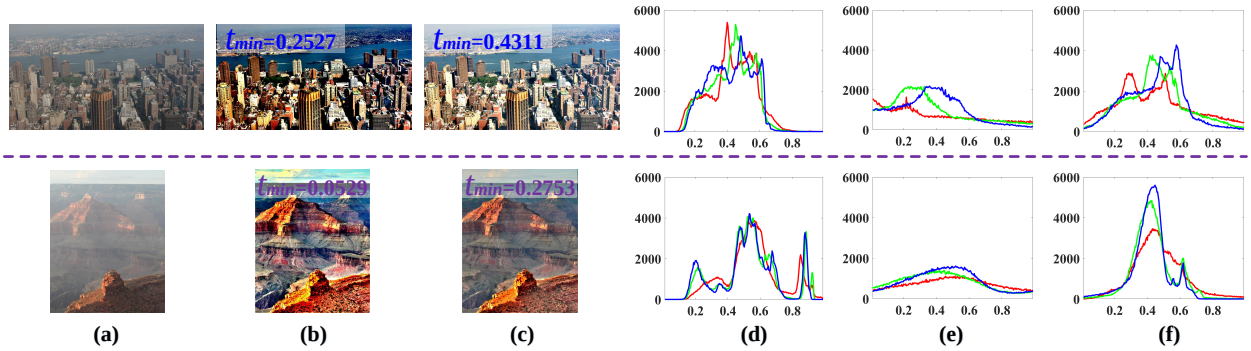

Fig. 4. Image dehazing performance comparison between setting $t_{min} = t_{al}$ (Eq. 21) and using GSS (Eq. 22) to determine t_{min} on two sample images. **(a)**: Hazy images. **(b)**: Results restored by IDE by setting $t_{min} = t_{al}$. **(c)**: Results restored by IDE by using GSS to find t_{min}. **(d)**: Histograms of (a). **(e)**: Histograms of (b). **(f)**: Histograms of (c).

where

$$\begin{cases} \lambda_1 = \hat{A} \cdot \ln(t_{min}) \\ \lambda_2(x,y) = \ln(t_{min}) \cdot (\hat{I}(x,y) + \hat{A} \cdot p_2 - \hat{A}) - \frac{1}{2} \cdot \hat{A} \cdot \ p_1 \\ \lambda_3(x,y) = p_2 \cdot \ln(t_{min}) \cdot \left(\hat{I}(x,y) - \hat{A}\right). \end{cases} \tag{16}$$

As a standard unary quadratic equation, Eq. 15 has two solutions. Since $\hat{t} \in [0,1]$, the negative solution is omitted and the only reasonable solution is

$$\hat{t}(x,y) = \frac{-\lambda_2(x,y) - \sqrt{(\lambda_2(x,y))^2 - 4 \cdot \lambda_1 \cdot \lambda_3(x,y)}}{2 \cdot \lambda_1}. \tag{17}$$

Previously, it was assumed that the transmission $\hat{t}(x,y)$ in a local patch is a constant. However, this approximation sometimes leads to depth discontinuities. To avoid this negative effect, guided filter (GF) [52] is employed:

$$\hat{t} = \mathrm{F}\left\{ \frac{-\lambda_2 - \sqrt{(\lambda_2)^2 - 4 \cdot \lambda_1 \cdot \lambda_3}}{2 \cdot \lambda_1} \right\}, \tag{18}$$

where $\mathrm{F}(\cdot)$ denotes the GF operator. According to Eq. 16, there are five parameters, i.e., $\ln(t_{min})$, $\hat{A}$, $\hat{I}$, p_1, and p_2, that are required to compute λ_1, λ_2, and λ_3 in Eq. 18. Therefore, Eq. 18 can be abbreviated as a function of the five parameters for clarity.

$$\hat{t}(x,y) = \Phi(\ln(t_{min}), \hat{A}, \hat{I}(x,y), p_1, p_2). \tag{19}$$

C. Scene Albedo Recovery

Substituting Eq. 19 and $\boldsymbol{A}$ estimated via [17] into EASM (Eq. 8), the scene albedo recovery formula (SARF) used for dehazing and exposure is expressed as:

$$\begin{aligned} \boldsymbol{\rho}(x,y) &= \mathrm{SF}(\boldsymbol{A}, \boldsymbol{I}, \ln(t_{min}), \hat{A}, \hat{I}(x,y), p_1, p_2) \\ &= \frac{\ln(t_{min})}{\ln\left(\Phi(\ln(t_{min}), \hat{A}, \hat{I}(x,y), p_1, p_2)\right)} \\ &\cdot \left(1 + \frac{\boldsymbol{I}(x,y) - \boldsymbol{A}}{\boldsymbol{A} \cdot \Phi(\ln(t_{min}), \hat{A}(x,y), \hat{I}, p_1, p_2)}\right), \end{aligned} \tag{20}$$

where $\mathrm{SF}(\cdot)$ is the abbreviation of SARF. Note that $\mathrm{SF}(\cdot)$ is a function of seven parameters, where $\boldsymbol{I}$ is the hazy input, $\boldsymbol{A}$ can be easily estimated via [17], $\hat{I}$ and $\hat{A}$ can be calculated by Eq. 10, the values of p_1 and p_2 have been optimized previously, and t_{min} is the only unknown parameter that remains unsolved.

Following the fact that the position of the atmospheric light usually corresponds to the pixel with the largest scene depth in the whole image [31], the most intuitive way to obtain t_{min} is to initialize its value as the transmission of the atmospheric light t_{al}. Note that t_{al} can be obtained by transforming Eq. 12, thus

$$t_{min} = t_{al} = \frac{\hat{I}(x_0,y_0) - \hat{A}}{\hat{A} \cdot (\frac{\ln(\hat{t}(x_0,y_0))}{2 \cdot \ln(t_{min})} - 1)} = \frac{2 \cdot \left(\hat{A} - \hat{I}(x_0,y_0)\right)}{\hat{A}}, \tag{21}$$

where (x_0, y_0) is the coordinate of atmospheric light. We remark that the employed GWA has a limitation, i.e., when a local patch contains the sky or single colour parts, the average albedo of this local patch should be different from the value (0.5) we set in Eq. 11. In these cases, t_{al} may be error-estimated. To find a suitable value of t_{min}, a global stretch strategy (GSS) is designed. It makes use of the information of the whole image instead of a pixel to determine t_{min}. Therefore, a global optimum result preventing over-enhancement and over-saturation can be attained. Formally, GSS is expressed as

$$\begin{aligned} &t_{min} = \\ &\mathrm{argmin}\left\{ \Psi\left(\mathrm{SF}(\boldsymbol{A}, (\boldsymbol{I}) \downarrow^{\delta}, \ln(t_{min}), \hat{A}, (\hat{I}) \downarrow^{\delta}, p_1, p_2)\right) - \varepsilon \right\}, \end{aligned} \tag{22}$$

where $\downarrow^{\delta}$ is a down-sampling operator with coefficient $\delta = 4$, $\Psi(\cdot)$ is the saturation operator, and ε is the pre-set saturation of dehazed results. In this work, we clip 2% of the pixel values in the shadows and in the highlights, i.e., setting $\varepsilon = 0.02$. The designed GSS is a 1-D search problem and can be solved via the golden section method (GS). Once t_{min} was computed via GS, the transmission and the haze-free results can be directly generated via Eq. 18 and SARF (Eq. 20), respectively. Fig. 4 shows the recovery results and the corresponding histograms using IDE with $t_{min} = t_{al}$ and GSS on two examples. As expected, GSS makes up the limitation of GWA, and it is

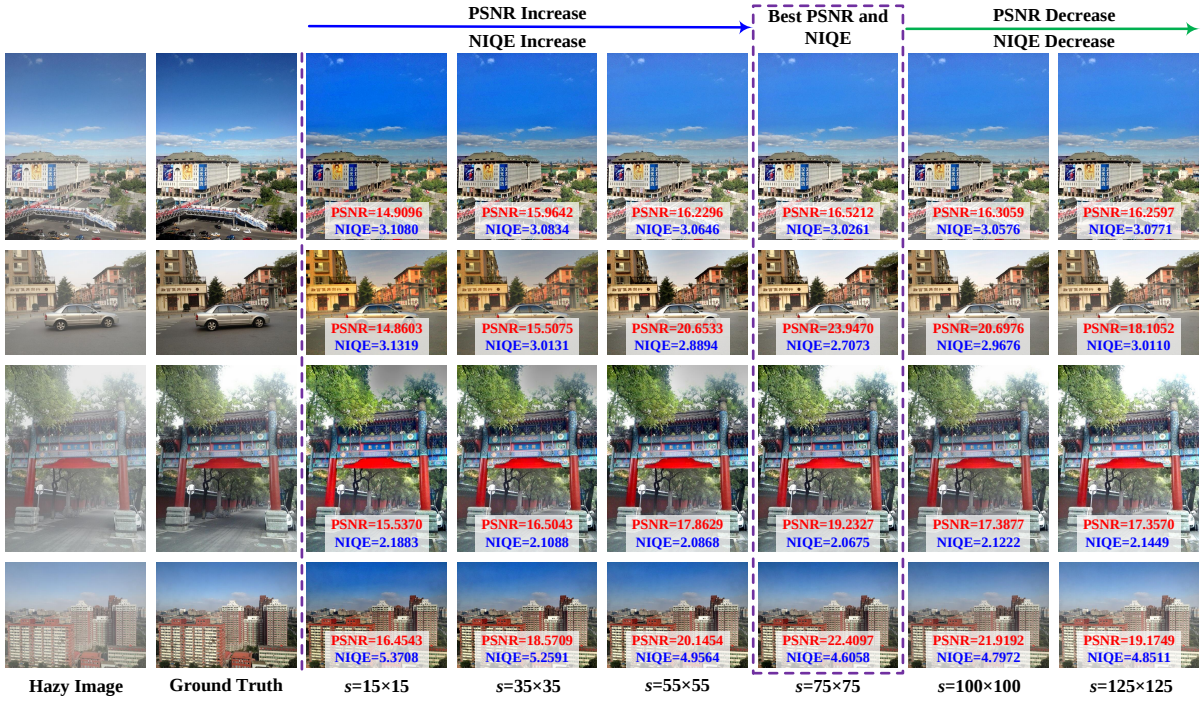

Fig. 5. Image dehazing and exposing using IDE with different local patch sizes s.

Algorithm 1 Proposed IDE

Input: Hazy image $\boldsymbol{I}$.

Pre-set parameters: $p_1 = -0.397$, $p_2 = 0.07747$, $\varepsilon = 0.02$, $\delta = 4$, $s = 75 \times 75$.

Begin

1. Locate the atmospheric light $\boldsymbol{A}$ from $\boldsymbol{I}$ via [17].
2. Calculate the $\hat{I}$ and $\hat{A}$ via Eq. 10.
3. Search t_{min} via GSS (Eq. 22) with GS.
4. Estimate the transmission t via Eq. 18.
5. Restore the scene albedo $\boldsymbol{\rho}$ via SARF (Eq. 20).

End

Output: Enhanced result $\boldsymbol{\rho}$.

able to achieve a high-quality restoration by maximizing the contrast with minimal information loss. For clarity, the step-by-step procedure of IDE proposed in this paper is outlined in Algorithm I.

IV. Experiments

In this section, experiments were conducted to evaluate the performance of the proposed EASM and IDE. They were implemented in MATLAB2016b on a PC with an Intel(R) Core (TM) i5-7200UCPU@ 2.50GHz 16.00 GB RAM. The parameters used in the available techniques for comparison were optimized according to the corresponding references, and the hazy images used in the experiments were collected from real-world or publicly available datasets.

A. Local patch size

A key parameter of IDE is the size of the local patch s. On one hand, GWA employed in IDE becomes more reliable with a larger s. On the other hand, the assumption that the transmission is a constant within a local patch loses its utility for a larger s. To determine an appropriate local patch size, we selected four samples containing both hazy images and ground truth from Realistic Single Image Dehazing (RESIDE) datasets [53] as examples and tested them by the proposed IDE with different patch sizes. During the experiment, peak signal-to-noise ratio (PSNR) and natural image quality evaluator (NIQE) [54] were used to quantitatively evaluate the test results, as illustrated in Fig. 5. Note that a higher PSNR means that the dehazed result is more similar to the ground truth, and a smaller NIQE represents that the restored image is more realistic and natural. It can be easily concluded from this figure that $s = 75 \times 75$ gives the best results. Here we remark that $s = 75 \times 75$ may not be the best size for all images, but it is a pretty robust empirical size that can be used on all types of images straightforwardly. In following experiments, the results recovered by IDE are all based on $s = 75 \times 75$.

B. Robustness Test on ASM and EASM

IDE is based on the EASM proposed in this work. The difference between ASM and EASM is the newly introduced parameter, i.e., the light absorption coefficient α. To investigate the influence of α on the recovery performance, we performed a robustness test on ASM and EASM, and the results are shown in Fig. 6. Two hazy examples, one with mist and the other with dense haze, were employed in the test, as shown in Fig. 6(a). Fig. 6(b) shows the recovered results using ASM+GWA and EASM+GWA. It is observed that the EASM-GWA-based dehazing exhibits significantly better restoration performance and has moderate exposure to improve the contrast for dim scenes. Moreover, we also used the well-

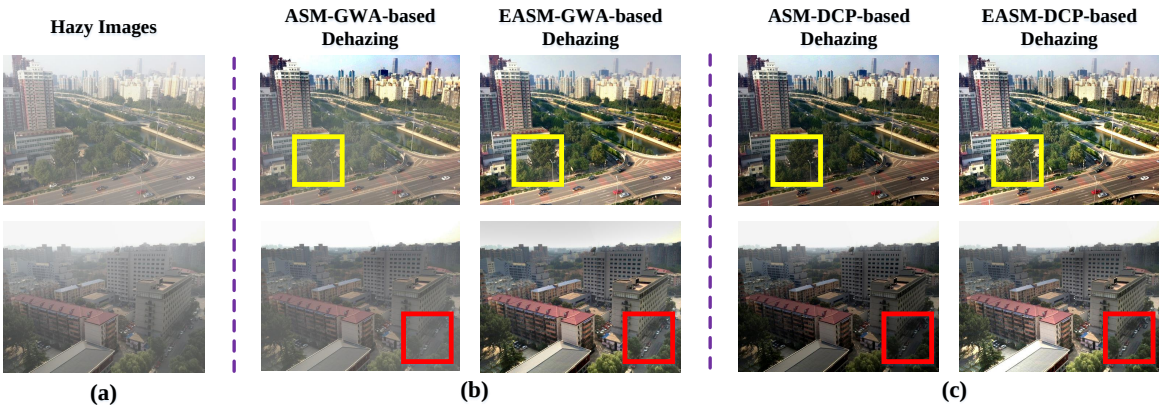

Fig. 6. Robustness test on ASM and EASM. **(a)**: Hazy images. **(b)**: Results comparisons between ASM-GWA-based dehazing and EASM-GWA-based dehazing. **(c)**: Results comparisons between ASM-DCP-based dehazing and EASM-DCP-based dehazing. In this test, GSS is employed to search the minimum transmission in EASM.

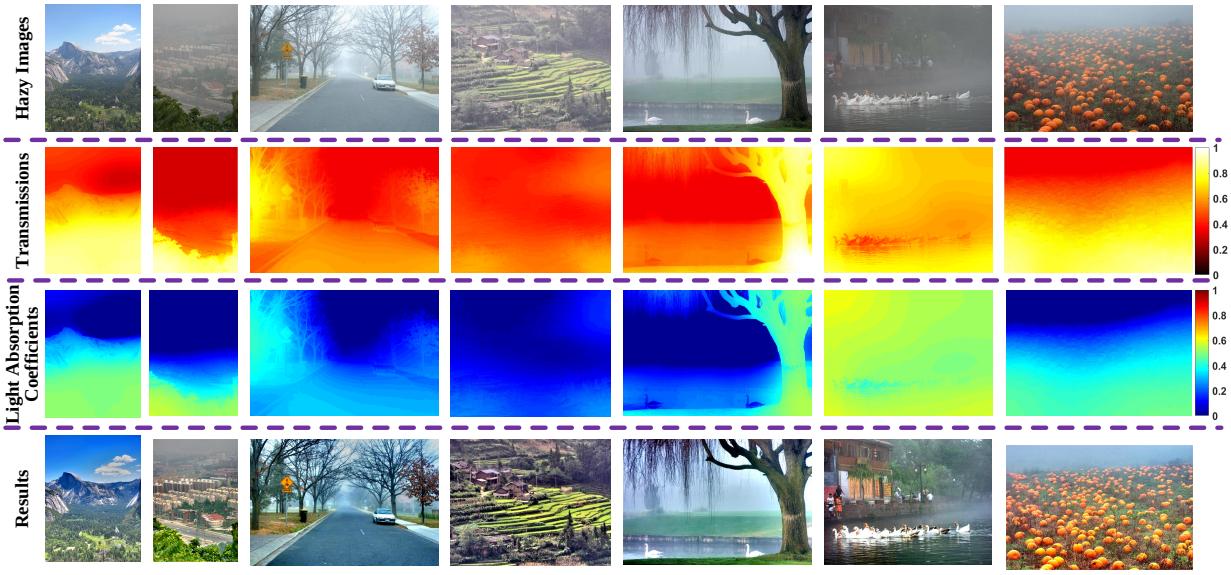

Fig. 7. Recovery results of IDE on different types of outdoor hazy images.

known DCP to test the two models. As shown in Fig. 6(c), the comparison results are similar. This reveals that EASM serves as a better model for image dehazing.

C. Evaluation of IDE

Being able to handle hazy images in complex environments is the prerequisite for becoming a "good" candidate for dehazing techniques. Therefore, we used several different types of hazy images collected from the real world and used them to test the proposed IDE. The hazy images, the transmissions, the light absorption coefficients, and the corresponding recovery results are illustrated in Fig. 7. As observed from the figure, IDE is capable of thoroughly removing the haze cover in the hazy images, while the estimated transmissions and the light absorption coefficients are sharp and consistent with the real situations. Moreover, thanks to the exposure property inherited from EASM, IDE is able to clearly unveil the hidden details and truly restitute the colours as they should be.

D. Qualitative comparison between IDE and other state-of-the-art techniques on real-world images

In this subsection, five images collected from the real world with different haze levels are selected to facilitate the comparison between IDE and the most representative or state-of-the-art techniques, including fusion-based DEFADE [10] (TIP 2015), learning-based DehazeNet [32] (TIP 2016), learning-based MSCNN [33] (ECCV 2016), learning-based EPDN [55] (CVPR 2019), prior-based HL [20] (TPAMI 2020), and prior-based IDGCP [21] (TIP 2020). Fig. 8(a) shows the five hazy samples; Figs. 8(b) to (h) give the recovered results using different dehazing techniques.

As seen in Fig. 8(b), DEFADE amplifies the details buried by haze to some extent, but the results of the first three examples seem to be too dim. Figs. 8(c) and 8(d) show that DehazeNet and MSCNN work quite well on misty images, but they cannot completely remove the haze scenes with dense haze (see example E5). For EPDN, on the contrary, it is able to

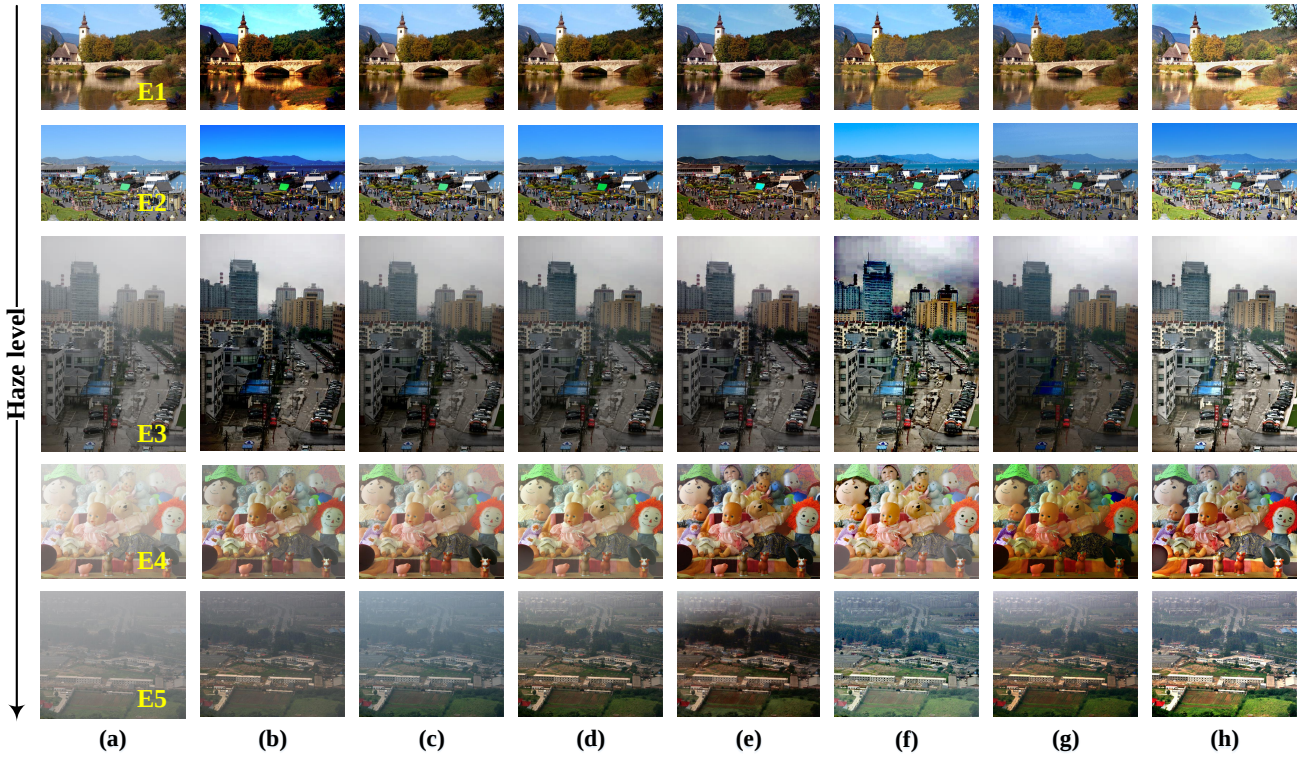

Fig. 8. Qualitative comparison between the proposed IDE and the state-of-the-art techniques on real-world images. **(a)**: Hazy Images. **(b)**: DEFADE. **(c)**: DehazeNet. **(d)**: MSCNN. **(e)**: EPDN. **(f)**: HL. **(g)**: IDGCP. **(h)**: IDE.

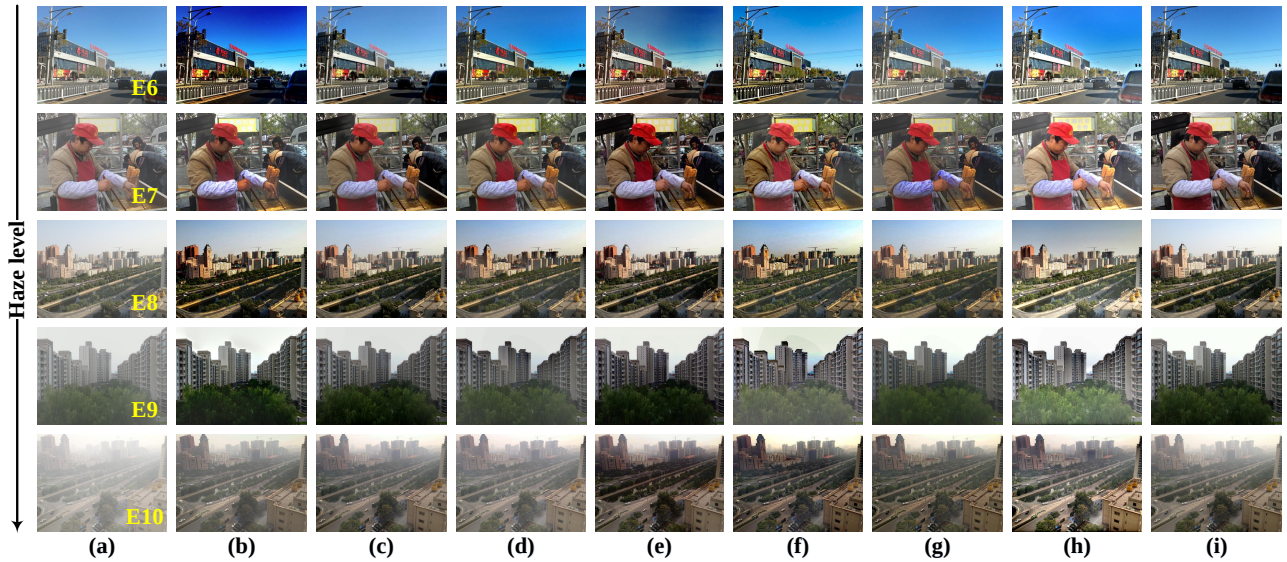

Fig. 9. Qualitative comparison between the proposed IDE and the state-of-the-art techniques on synthetic images. **(a)**: Hazy images. **(b)**: DEFADE. **(c)**: DehazeNet. **(d)**: MSCNN. **(e)**: EPDN. **(f)**: HL. **(g)**: IDGCP. **(h)**: IDE. **(i)**: Ground truth.

produce a good dehazed results for most cases except the mist images (see the E2 example in Fig. 8(e)). Due to the introduced postprocessing operator (namely, linear contrast stretch), HL can remove the haze and improve the global contrast for the given images. However, due to the limitations of the employed haze-lines prior, HL introduces some noise in sky regions, as shown in example E3 in Fig. 8(f). Although high-quality haze-free results of the given examples can be obtained by IDGCP, the recovered results appear to be too dim (see E3 and E4 examples in Fig. 8(g)). In comparison, as shown in Fig. 8(h), IDE avoids almost all of the negative effects and truly reflects the underlying scene content, thereby resulting in better visual quality.

TABLE I
QUANTITATIVE COMPARISON BETWEEN IDE AND OTHER STATE-OF-THE-ART TECHNIQUES ON THE RECOVERED IMAGES SHOWN IN FIG. 8 AND FIG. 9 USING R, NIQE, FADE, AND PSNR.

Metrics	Images	DEFADE [10]	DehazeNet [32]	MSCNN [33]	EPDN [55]	HL [20]	IDGCP [21]	IDE
R	E1	1.2152	0.9708	0.8851	1.0985	0.9862	0.9330	**1.2978**
	E2	0.9045	1.0462	0.9512	1.1470	1.2647	1.2440	**1.3440**
	E3	1.5791	1.1730	1.2476	1.4176	**3.4257**	1.0122	2.2004
	E4	1.7710	1.7478	2.2753	2.4273	3.4496	2.1383	**3.5030**
	E5	1.6767	1.6088	2.6613	2.4337	6.4164	2.7989	**6.8946**
	E6	1.3837	1.2403	1.0910	1.3402	1.6806	0.9557	**1.7116**
	E7	1.4814	1.3507	1.3045	1.4712	1.8961	0.9793	**1.9251**
	E8	1.5179	1.3247	1.1516	1.3714	1.4988	0.9339	**1.7697**
	E9	1.7198	1.4300	1.2902	1.5189	2.0388	0.9330	**2.0698**
	E10	1.7798	1.7976	1.8746	2.3179	2.9663	1.3443	**4.1621**
NIQE	E1	2.6659	2.1580	1.9391	2.9641	2.0879	1.9204	**1.8809**
	E2	4.4383	3.2545	3.0897	3.6170	3.5514	2.5758	**2.2290**
	E3	2.7927	2.4056	2.3341	3.0666	2.5931	2.5862	**2.3128**
	E4	3.0047	2.9796	2.8267	3.0704	2.6594	3.0124	**2.6392**
	E5	3.2245	3.6894	3.2351	3.9601	2.5843	3.1489	**2.4405**
	E6	4.2357	3.5262	3.7389	3.6301	3.3294	3.6257	**3.2523**
	E7	2.0500	1.8159	1.9028	2.1065	1.7153	2.0677	**1.7008**
	E8	2.6568	2.1793	2.1772	2.4492	2.1297	2.1706	**2.1044**
	E9	3.1720	3.6955	3.7195	4.1508	3.7537	3.8750	**3.0059**
	E10	2.3058	2.1038	2.0556	2.8367	1.7351	1.8456	**1.7222**
FADE	E1	**0.2088**	0.3644	0.2473	0.2825	0.4983	0.4233	0.5144
	E2	**0.2672**	0.4614	0.3561	0.2496	0.2744	0.3767	0.4153
	E3	0.3018	0.5159	0.4524	0.4593	**0.1956**	0.8568	0.6075
	E4	0.7753	0.7047	0.4695	0.3470	0.4256	0.4161	**0.3436**
	E5	0.8477	0.9807	0.4387	0.3677	0.3601	0.4450	**0.2780**
	E6	**0.2283**	0.3858	0.3500	0.3076	0.2947	0.4503	0.4065
	E7	0.4035	0.2826	0.3637	**0.2123**	0.2403	0.4131	0.4025
	E8	**0.3570**	0.5973	0.7275	0.4974	0.5160	0.7778	0.7647
	E9	0.5619	0.6275	0.8125	**0.4989**	0.6200	0.7925	0.8949
	E10	0.9993	0.8427	0.8881	0.3778	0.4639	0.5683	**0.3953**
PSNR	E6	15.7884	**22.9553**	19.8269	18.5936	18.7813	17.6215	18.1126
	E7	21.4840	**24.6080**	22.0188	21.3633	18.4292	20.2170	15.3905
	E8	17.7240	24.3185	20.3312	**24.3344**	17.7444	22.4034	15.0865
	E9	**27.5315**	24.7915	18.5315	23.3222	14.9130	22.5959	17.8418
	E10	23.2838	**27.7594**	21.7596	15.5834	17.4352	19.4440	18.7280

TABLE II
QUANTITATIVE COMPARISON BETWEEN IDE AND OTHER STATE-OF-THE-ART TECHNIQUES ON ALL THE IMAGES (MEAN VALUE) IN I-HAZE AND O-HAZE DATASETS USING R, NIQE, FADE, AND PSNR.

Dataset	Technique	R	NIQE	FADE	PSNR
I-HAZE	DEFADE	2.0494	3.8314	1.0555	15.7328
	DehazeNet	1.4546	4.2853	1.1239	15.0288
	MSCNN	1.5371	4.3510	1.6312	**16.5437**
	EPDN	2.2351	3.7717	0.7503	14.9531
	HL	3.3434	3.8140	0.6368	14.4640
	IDGCP	1.4945	4.4293	1.4780	16.0996
	IDE	**3.4282**	**3.4009**	**0.6175**	15.7729
O-HAZE	DEFADE	1.8544	2.5157	0.3353	15.2376
	DehazeNet	1.2774	2.6616	0.8733	15.4253
	MSCNN	1.6479	2.5310	0.5239	16.6218
	EPDN	2.3063	2.9849	0.3361	**16.8753**
	HL	3.4810	2.5311	0.3398	13.1370
	IDGCP	1.8023	2.5994	0.5495	15.7068
	IDE	**3.6363**	**2.4359**	**0.3133**	14.1891

E. Qualitative comparison between IDE and other state-of-the-art techniques on synthetic images

To fully evaluate the proposed IDE, we further conducted a comparison between IDE and other state-of-the-art techniques on RESIDE datasets [53]. These samples include both hazy images and the corresponding ground truth images. The comparison is illustrated in Fig. 9. As shown in Figs. 9(b) and 9(e), DEFADE and EPDN are able to uncover the target contour for most examples, but the dark areas of the recovered images seem to be over-saturated (see examples E6, E8, and E9). DehazeNet and MSCNN are able to produce attractive results for the given mist images, as shown in Figs. 9(c) and 9(d). However, they are not able to deal with images with dense haze, see example E10. According to example E9 in Fig. 9(f), HL exhibits limited performance on scenes with gray white colours. As observed in Fig. 9(g), IDGCP achieves visually pleasing results for most given images. However, due to the limitations of ASM, its results may appear to be darker than they should be. In comparison, IDE restitutes the details and contours well and retains the color consistency. Most importantly, IDE can not only eliminate haze interference but also compensate for illumination in dim scenes (see Fig. 9(h)).

F. Quantitative comparison between IDE and state-of-the-art techniques

Because of subjective judgement differences among different viewers, it is difficult to fairly rank the different techniques in terms of recovery quality. Therefore, four commonly used metrics, i.e., the mean ratio of the gradients at the visible edges (R) [56], fog aware density evaluator (FADE) [10], and the aforementioned NIQE [54] and PSNR, are employed to facilitate a quantitative comparison. Among them, R, NIQE, and FADE are non-reference indicators, while PSNR is a reference indicator that needs ground truth to participate in evaluation.

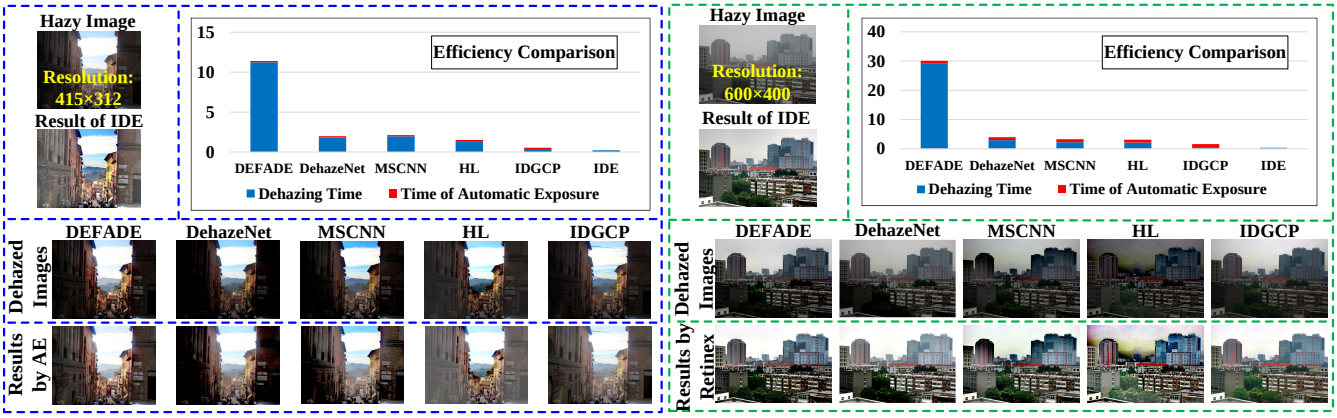

Fig. 11. Comparison of the processing time and visual quality between IDE and other state-of-the-art techniques with different post-processing methods (Retinex [46] and automatic exposure).

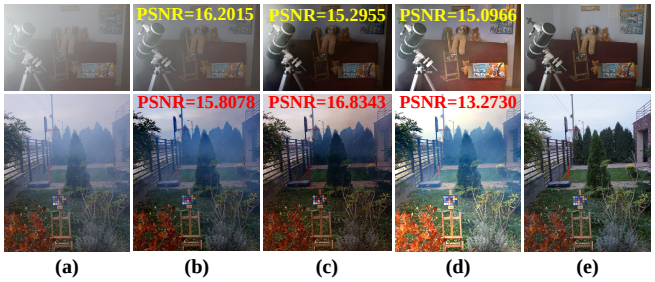

Fig. 10. Quantitative comparison between the proposed IDE and the two techniques with the best PSNR scores (MSCNN and EPDN) on two example images from I-HAZE and O-Haze Datasets. **(a)**: Hazy Images. **(b)**: MSCNN. **(c)**: EPDN. **(d)**: IDE. **(e)**: Ground Truth.

In general, a greater R represents richer information contained in the image, and a smaller FADE indicates less mist residue in the dehazed result.

Table I summarizes the scores of the four metrics on the images restored using different techniques shown in Figs. 8 and 9. Note that we did not give the PSNR values for the dehazed images in Fig. 8 since the ground truth of real-world hazy image is unavailable. As can be concluded from the table, it is not surprising that IDE achieves the highest R scores for almost all images, which is mainly due to the exposure ability inherited from EASM. Moreover, IDE also has the best score for NIQE, which signifies that it achieves the highest restoration quality. For FADE and PSNR, the IDE scores are not the best for all given examples. This is because the exposure makes the recovery results brighter than the ground truth images. The bright scenes may be mistaken as haze residue by FADE and magnify the difference between the dehazed results and the ground truth images, which reduces the PSNR score.

To make the comparison more convincing, we further tested IDE and other comparable algorithms on all the images in two datasets, O-HAZE [57] and I-HAZE [58]. The mean values of the four metrics for all the images are reported in Table II. As shown, it is clear that IDE outperforms state-of-the-art techniques in terms of R, NIQE, and FADE, which proves the superiority of the proposed IDE. Although IDE does not have the best PNSR value, as discussed before, this is mainly due to the exposing feature embedded in the IDE which brightens the scene and increases the differences between the recovery results and the ground truth image. Nevertheless, the resultant results are clearer than the ground truth images; thus, it is actually not a drawback. To prove that, we conducted experiments on two example images from I-HAZE and O-HAZE by using the techniques with the best PNSR scores (MSCNN and EPDN) and the proposed IDE. The results are illustrated in Fig. 10. As can be concluded from this figure, the recovery quality of IDE is remarkably better than that of other algorithms despite the lower PNSR score.

G. Comparison of Running Time

Recall that in Fig. 2, it is illustrated that the real scene albedos can be obtained by applying Retinex to the results obtained by ASM-based dehazing techniques. Although ASM embedded in the algorithms usually causes a dim effect in the recovery results, the dim effect can be compensated by post-processing such as Retinex [46]. Here, we remark that the proposed IDE naturally possesses both dehazing and exposure abilities, and it does not need a postprocessing to improve the quality. Therefore, it needs a shorter processing time than other state-of-the-art techniques. Fig. 11 illustrates the comparison of IDE and other state-of-the-art dehazing algorithms combined with postprocessing by Retinex and automatic exposure (AE) in terms of visual quality and processing time. When computing the processing time, the atmospheric light of different techniques was initially set as the same value, and all simulations were executed in MATLAB with the same environment to ensure fairness. Note that EPDN was not included in the comparison because its code is implemented in Python, whereas the remaining techniques are all conducted in MATLAB. It can be easily concluded from Fig. 11 that IDE achieves the most realistic and natural results for given images with nonuniform illumination or uniform illumination. Moreover, IDE uses less processing time than others as well. When the processing time of Retinex or AE is considered, there is no doubt that IDE is significantly faster than all the other techniques.

To further demonstrate its fast processing feature, IDE was also compared with state-of-the-art techniques on the images in Fig. 8, where images E1 and E2 were tested with various resolutions and images E3 to E5 were tested with the same resolutions. The running times are illustrated in Table III and Table IV, respectively. Note that the symbol "-" in the tables denotes "out of memory". As can be seen from these tables, the running speed of IDE is much faster than those of the other compared approaches regardless of the resolution and the image. Therefore, the proposed IDE can serve as an excellent candidate that provides both the dehazing and exposure services for real-time systems.

V. Conclusion

In this paper, by introducing a light absorption coefficient α into atmospheric scattering model (ASM), an enhanced ASM (EASM) was obtained. The main advantage of EASM is that it can overcome the dim effect caused by ASM and better model hazy scenes. Benefitting from this EASM, a gray-world-assumption-based technique called IDE was then developed to enhance the visibility of hazy images. In contrast to previous prior-based and learning-based techniques, IDE is based on a global stretch strategy, and it can simultaneously dehaze and expose single hazy images without the needs of post-processing. Moreover, IDE does not require any training procedure or extra information related to scene depth, and the tools or calculation formula used in IDE are all simple operators, which ensures its high efficiency and strong robustness. Experiments verify that EASM has a better modelling ability for hazy images compared to ASM, and the resultant IDE is superior over most state-of-the-art techniques in terms of both the processing efficiency and recovery quality.

References

[1] R. Cong, J. Lei, H. Fu, M.-M. Cheng, W. Lin, and Q. Huang, "Review of visual saliency detection with comprehensive information," *IEEE Transactions on Circuits and Systems for Video Technology*, vol. 29, no. 10, pp. 2941–2959, 2019.

[2] C. Li, R. Cong, J. Hou, S. Zhang, Y. Qian, and S. Kwong, "Nested network with two-stream pyramid for salient object detection in optical remote sensing images," *IEEE Transactions on Geoscience and Remote Sensing*, vol. 57, no. 11, pp. 9156–9166, 2019.

[3] T. Kim and J. Paik, "Adaptive contrast enhancement using gain-controllable clipped histogram equalization," *IEEE Transactions on Consumer Electronics*, vol. 54, no. 4, pp. 1803–1810, 2008.

[4] K. J. Zuiderveld, "Contrast limited adaptive histogram equalization," *Graphics gems*, pp. 474–485, 1994.

[5] E. H. Land and J. J. Mccann, "Lightness and retinex theory," *Journal of the Optical Society of America*, vol. 61, no. 1, pp. 1–11, 1971.

[6] H. Xu, G. Zhai, X. Wu, and X. Yang, "Generalized equalization model for image enhancement," *IEEE Transactions on Multimedia*, vol. 16, no. 1, pp. 68–82, 2014.

[7] W. Cai, Y. Liu, M. Li, L. Cheng, and C. Zhang, "A self-adaptive homomorphic filter method for removing thin cloud," in *2011 19th International Conference on Geoinformatics*, 2011, pp. 1–4.

[8] C. O. Ancuti, C. Ancuti, and P. Bekaert, "Effective single image dehazing by fusion," in *2010 IEEE International Conference on Image Processing*, 2010, pp. 3541–3544.

[9] C. O. Ancuti and C. Ancuti, "Single image dehazing by multi-scale fusion," *IEEE Transactions on Image Processing*, vol. 22, no. 8, pp. 3271–3282, 2013.

[10] L. K. Choi, J. You, and A. C. Bovik, "Referenceless prediction of perceptual fog density and perceptual image defogging," *IEEE Transactions on Image Processing*, vol. 24, no. 11, pp. 3888–3901, 2015.

[11] S. G. Narasimhan and S. K. Nayar, "Contrast restoration of weather degraded images," *IEEE Transactions on Pattern Analysis and Machine Intelligence*, vol. 25, no. 6, pp. 713–724, 2003.

[12] J. Kopf, B. Neubert, B. Chen, M. Cohen, D. Cohen-Or, O. Deussen, M. Uyttendaele, and D. Lischinski, "Deep photo : model-based photograph enhancement and viewing," *ACM transactions on graphics*, vol. 27, no. 5, 2008, article Number: 116.

[13] N. Hautiere, J. Tarel, and D. Aubert, "Towards fog-free in-vehicle vision systems through contrast restoration," in *2007 IEEE Conference on Computer Vision and Pattern Recognition*, 2007, pp. 1–8.

[14] Y. Y. Schechner, S. G. Narasimhan, and S. K. Nayar, "Instant dehazing of images using polarization," in *Proceedings of the 2001 IEEE Computer Society Conference on Computer Vision and Pattern Recognition. CVPR 2001*, vol. 1, 2001, pp. I–I.

[15] R. Cong, J. Lei, H. Fu, J. Hou, Q. Huang, and S. Kwong, "Going from RGB to RGBD saliency: A depth-guided transformation model," *IEEE Transactions on Cybernetics*, vol. 50, no. 8, pp. 3627–3639, 2020.

[16] Z. Chen, R. Cong, Q. Xu, and Q. Huang, "DPANet: Depth potentiality-aware gated attention network for RGB-D salient object detection," *IEEE Transactions on Image Processing*, 2020.

[17] K. He, J. Sun, and X. Tang, "Single image haze removal using dark channel prior," *IEEE Transactions on Pattern Analysis and Machine Intelligence*, vol. 33, no. 12, pp. 2341–2353, 2011.

[18] W. Wang, X. Yuan, X. Wu, and Y. Liu, "Fast image dehazing method based on linear transformation," *IEEE Transactions on Multimedia*, vol. 19, no. 6, pp. 1142–1155, 2017.

[19] D. Berman, T. Treibitz, and S. Avidan, "Non-local image dehazing," in *2016 IEEE Conference on Computer Vision and Pattern Recognition (CVPR)*, 2016, pp. 1674–1682.

[20] ——, "Single image dehazing using haze-lines," *IEEE Transactions on Pattern Analysis and Machine Intelligence*, vol. 42, no. 3, pp. 720–734, 2020.

[21] M. Ju, C. Ding, Y. J. Guo, and D. Zhang, "Idgcp: Image dehazing based on gamma correction prior," *IEEE Transactions on Image Processing*, vol. 29, pp. 3104–3118, 2020.

[22] P. Liu, S. Horng, J. Lin, and T. Li, "Contrast in haze removal: Configurable contrast enhancement model based on dark channel prior," *IEEE Transactions on Image Processing*, vol. 28, no. 5, pp. 2212–2227, 2019.

[23] T. M. Bui and W. Kim, "Single image dehazing using color ellipsoid prior," *IEEE Transactions on Image Processing*, vol. 27, no. 2, pp. 999–1009, 2018.

[24] M. Ju, C. Ding, D. Zhang, and Y. J. Guo, "Bdpk: Bayesian dehazing using prior knowledge," *IEEE Transactions on Circuits and Systems for Video Technology*, vol. 29, no. 8, pp. 2349–2362, 2019.

[25] M. Yang, J. Liu, and Z. Li, "Superpixel-based single nighttime image haze removal," *IEEE Transactions on Multimedia*, vol. 20, no. 11, pp. 3008–3018, 2018.

[26] M. Ju, C. Ding, D. Zhang, and Y. J. Guo, "Gamma-correction-based visibility restoration for single hazy images," *IEEE Signal Processing Letters*, vol. 25, no. 7, pp. 1084–1088, 2018.

[27] R. Fattal, "Dehazing using color-lines," *ACM Trans. Graph.*, vol. 34, no. 1, Dec. 2015. [Online]. Available: https://doi.org/10.1145/2651362

[28] S. Huang, J. Ye, and B. Chen, "An advanced single-image visibility restoration algorithm for real-world hazy scenes," *IEEE Transactions on Industrial Electronics*, vol. 62, no. 5, pp. 2962–2972, 2015.

[29] L. He, J. Zhao, N. Zheng, and D. Bi, "Haze removal using the difference-structure-preservation prior," *IEEE Transactions on Image Processing*, vol. 26, no. 3, pp. 1063–1075, 2017.

[30] Y. Gao, H. Hu, B. Li, Q. Guo, and S. Pu, "Detail preserved single image dehazing algorithm based on airlight refinement," *IEEE Transactions on Multimedia*, vol. 21, no. 2, pp. 351–362, 2019.

[31] Q. Zhu, J. Mai, and L. Shao, "A fast single image haze removal algorithm using color attenuation prior," *IEEE Transactions on Image Processing*, vol. 24, no. 11, pp. 3522–3533, 2015.

[32] B. Cai, X. Xu, K. Jia, C. Qing, and D. Tao, "Dehazenet: An end-to-end system for single image haze removal," *IEEE Transactions on Image Processing*, vol. 25, no. 11, pp. 5187–5198, 2016.

[33] W. Ren, S. Liu, H. Zhang, J. Pan, X. Cao, and M.-H. Yang, "Single image dehazing via multi-scale convolutional neural networks," in *Computer Vision – ECCV 2016*, B. Leibe, J. Matas, N. Sebe, and M. Welling, Eds. Cham: Springer International Publishing, 2016, pp. 154–169.

[34] B. Li, X. Peng, Z. Wang, J. Xu, and D. Feng, "Aod-net: All-in-one dehazing network," in *2017 IEEE International Conference on Computer Vision (ICCV)*, 2017, pp. 4780–4788.

TABLE III
RUNNING TIME OF DIFFERENT TECHNIQUES ON THE FIRST TWO EXAMPLES WITH VARIOUS RESOLUTIONS IN FIG. 8 (UNIT: SECONDS).

Images	Resolutions	DEFADE [10]	DehazeNet [32]	MSCNN [33]	HL [20]	IDGCP [21]	IDE
E1	256 × 384	13.0348	1.07751	1.2045	1.7967	0.5939	**0.1451**
	512 × 768	27.4248	4.2678	4.5800	3.0726	0.7331	**0.2950**
	768 × 1152	115.76652	9.4034	8.5753	6.6644	1.1503	**0.6175**
	1024 × 1536	–	15.8749	15.4956	11.9515	1.8720	**0.8551**
	1280 × 1920	–	25.1349	30.6724	21.5100	2.3538	**1.3124**
	1536 × 2304	–	52.9122	61.3071	–	3.5234	**1.9249**
E2	300 × 200	10.0950	0.6414	0.8373	1.2033	0.5150	**0.1409**
	600 × 400	29.6365	2.8086	2.2528	2.1108	0.6225	**0.2733**
	900 × 600	77.7777	5.7323	4.4987	3.6817	0.7961	**0.5040**
	1200 × 800	–	13.5196	7.1119	6.2196	1.0749	**0.7051**
	1500 × 1000	–	22.3706	14.3999	12.2489	1.4495	**1.0542**
	1800 × 1200	–	35.4206	19.8218	16.1178	2.2204	**1.1693**

TABLE IV
RUNNING TIME OF DIFFERENT TECHNIQUES ON THE LAST THREE EXAMPLES WITH SAME RESOLUTIONS IN FIG. 8 (UNIT: SECONDS).

Resolutions	Images	DEFADE [10]	DehazeNet [32]	MSCNN [33]	HL [20]	IDGCP [21]	IDE
200×200	E3	4.7569	0.9248	1.0446	1.1277	0.3439	**0.1194**
	E4	4.4179	1.0265	1.1462	0.9273	0.3035	**0.1151**
	E5	4.8049	0.8930	0.9704	1.0634	0.3145	**0.1102**
400×400	E3	15.3725	2.2587	2.0721	1.7021	0.4864	**0.1796**
	E4	14.5740	2.2418	2.3653	1.5902	0.4142	**0.1606**
	E5	14.8179	2.3331	2.2103	1.6628	0.4205	**0.1719**
800×800	E3	96.6034	7.2403	6.8287	3.7343	0.9600	**0.4751**
	E4	92.1863	7.1900	7.2329	3.9209	0.9591	**0.4954**
	E5	99.1112	7.4019	6.9582	3.7130	0.9386	**0.4748**
1600×1600	E3	–	31.2226	36.032	20.7245	2.5560	**1.4508**
	E4	–	35.8156	39.1132	22.8633	2.9662	**1.3870**
	E5	–	33.3734	38.4135	21.7018	2.7310	**1.3555**
3200×3200	E3	–	–	–	–	7.4621	**5.0028**
	E4	–	–	–	–	8.6998	**4.7896**
	E5	–	–	–	–	8.4207	**5.1690**

[35] A. Golts, D. Freedman, and M. Elad, "Unsupervised single image dehazing using dark channel prior loss," *IEEE Transactions on Image Processing*, vol. 29, pp. 2692–2701, 2020.

[36] C. Li, C. Guo, J. Guo, P. Han, H. Fu, and R. Cong, "Pdr-net: Perception-inspired single image dehazing network with refinement," *IEEE Transactions on Multimedia*, vol. 22, no. 3, pp. 704–716, 2020.

[37] W. Ren, L. Ma, J. Zhang, J. Pan, X. Cao, W. Liu, and M. Yang, "Gated fusion network for single image dehazing," in *2018 IEEE/CVF Conference on Computer Vision and Pattern Recognition*, 2018, pp. 3253–3261.

[38] Y. Song, J. Li, X. Wang, and X. Chen, "Single image dehazing using ranking convolutional neural network," *IEEE Transactions on Multimedia*, vol. 20, no. 6, pp. 1548–1560, 2018.

[39] Y. Pang, J. Xie, and X. Li, "Visual haze removal by a unified generative adversarial network," *IEEE Transactions on Circuits and Systems for Video Technology*, vol. 29, no. 11, pp. 3211–3221, 2019.

[40] X. Liu, Y. Ma, Z. Shi, and J. Chen, "Griddehazenet: Attention-based multi-scale network for image dehazing," 2019.

[41] Y. Pang, J. Nie, J. Xie, J. Han, and X. Li, "Bidnet: Binocular image dehazing without explicit disparity estimation," in *2020 IEEE/CVF Conference on Computer Vision and Pattern Recognition (CVPR)*, 2020, pp. 5930–5939.

[42] Y. Shao, L. Li, W. Ren, C. Gao, and N. Sang, "Domain adaptation for image dehazing," in *2020 IEEE/CVF Conference on Computer Vision and Pattern Recognition (CVPR)*, 2020, pp. 2805–2814.

[43] H. Hu, H. Zhang, Z. Zhao, B. Li, and J. Zheng, "Adaptive single image dehazing using joint local-global illumination adjustment," *IEEE Transactions on Multimedia*, vol. 22, no. 6, pp. 1485–1495, 2020.

[44] S. Santra and B. Chanda, "Single image dehazing with varying atmospheric light intensity," in *2015 Fifth National Conference on Computer Vision, Pattern Recognition, Image Processing and Graphics (NCVPRIPG)*, 2015, pp. 1–4.

[45] J. V. Anguita, M. Ahmad, S. Haq, J. Allam, and S. R. P. Silva, "Ultra-broadband light trapping using nanotextured decoupled graphene multilayers," *Science Advances*, vol. 2, no. 2, 2016. [Online]. Available: https://advances.sciencemag.org/content/2/2/e1501238

[46] X. Guo, Y. Li, and H. Ling, "Lime: Low-light image enhancement via illumination map estimation," *IEEE Transactions on Image Processing*, vol. 26, no. 2, pp. 982–993, 2017.

[47] M. Ju, Z. Gu, and D. Zhang, "Single image haze removal based on the improved atmospheric scattering model," *Neurocomputing*, vol. 260, pp. 180–191, 2017.

[48] G. Buchsbaum, "A spatial processor model for object colour perception," *Journal of the Franklin Institute*, vol. 310, no. 1, pp. 1–26, 1980.

[49] M. T. T. Nguyen, C. L. D. A. Mai, and N. M. Kwok, "Estimating image illuminant color based on gray world assumption," in *2011 4th International Congress on Image and Signal Processing*, vol. 2, 2011, pp. 989–993.

[50] R. Sethi and S. Indu, "Local enhancement of slic segmented underwater images using gray world based algorithm," in *2017 Ninth International Conference on Advances in Pattern Recognition (ICAPR)*, 2017, pp. 1–6.

[51] H. Li, L. Zhang, and H. Shen, "A perceptually inspired variational method for the uneven intensity correction of remote sensing images," *IEEE Transactions on Geoscience and Remote Sensing*, vol. 50, no. 8, pp. 3053–3065, 2012.

[52] K. He, J. Sun, and X. Tang, "Guided image filtering," *IEEE Transactions on Pattern Analysis and Machine Intelligence*, vol. 35, no. 6, pp. 1397–1409, 2013.

[53] B. Li, W. Ren, D. Fu, D. Tao, D. Feng, W. Zeng, and Z. Wang, "Benchmarking single-image dehazing and beyond," *IEEE Transactions on Image Processing*, vol. 28, no. 1, pp. 492–505, 2019.

[54] A. Mittal, R. Soundararajan, and A. C. Bovik, "Making a âĂIJcompletely blindâĂİ image quality analyzer," *IEEE Signal Processing Letters*, vol. 20, no. 3, pp. 209–212, 2013.

[55] Y. Qu, Y. Chen, J. Huang, and Y. Xie, "Enhanced pix2pix dehazing network," in *2019 IEEE/CVF Conference on Computer Vision and Pattern Recognition (CVPR)*, 2019, pp. 8152–8160.

[56] N. Hautiere, J. P. Tarel, D. Aubert, and E. Dumont, "Blind contrast enhancement assessment by gradient ratioing at visible edges.(report)," *Image Analysis and Stereology*, vol. 27, no. 2, pp. 87–95, 2011.

[57] C. O. Ancuti, C. Ancuti, R. Timofte, and C. De Vleeschouwer, "O-haze: A dehazing benchmark with real hazy and haze-free outdoor

images," in *2018 IEEE/CVF Conference on Computer Vision and Pattern Recognition Workshops (CVPRW)*, 2018, pp. 867–8678.
[58] C. O. Ancuti, C. Ancuti, R. Timofte, and C. D. Vleeschouwer, "I-haze: a dehazing benchmark with real hazy and haze-free indoor images," in *arXiv:1804.05091v1*, 2018.

Mingye Ju received a Bachelor degree in communication engineering from Nanjing University of Posts and Telecommunications, Nanjing, China, in 2010; a Master degree in signal processing from Tianjin University of Technology and Education, Tianjin, China, in 2013; a PH.D degree from Nanjing University of Posts and Telecommunications, Nanjing, China, in 2018; and a PH.D degree from Global Big Data Technologies Centre (GBDTC), University of Technology Sydney, Sydney, Australia, in 2020. He is currently a lecturer with the School of Internet of Things, Nanjing University of Posts and Telecommunication, Nanjing, China. Meanwhile, he is also a postdoctoral researcher at Nanjing University of Science and Technology. His research interests include computer vision and image processing.

Can Ding (M'16) received a Bachelor degree in Micro-electronics from Xidian University, Xi'an, China, in 2009; and a PH.D. degreed from Macquarie University, Sydney, Australia, in 2015. From 2012 to 2015, he was under the cotutelle agreement between Macquarie University, Australia and Xidian University, China. During this period, he was also with the Commonwealth Scientific and Industrial Research Organisation (CSIRO) DPaS Flagship, Marsfield, Australia. From 2015 to 2017, he was a post-doctoral research fellow in University of Technology Sydney (UTS), Sydney, Australia. He is currently a lecturer with the Global Big Data Technologies Centre (GBDTC), University of Technology Sydney (UTS), Sydney, Australia. He is the receipt of Australia Research Council (ARC) Discovery Early Career Researcher Award (DECRA) Fellow in 2020. His research interest is in the area of base station antennas, reconfigurable antennas, phase shifters, and fibres for wireless communication and sensing.

Wenqi Ren (M'18) Wenqi Ren received the Ph.D. degree from Tianjin University in 2017. From 2015 to 2016, he was a Joint-Training Ph.D. Student in electrical engineering and computer science with the University of California at Merced, Merced, CA, USA. He is currently an Assistant Professor with the Institute of Information Engineering, Chinese Academy of Sciences, China. His research interests include image/video analysis and enhancement, and related vision problems.

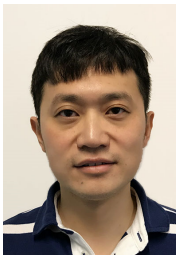

Yi Yang received the Ph.D. degree in computer science from Zhejiang University, Hangzhou, China, in 2010. He is currently a professor with University of Technology Sydney, Australia. He was a Post-Doctoral Research with the School of Computer Science, Carnegie Mellon University, Pittsburgh, PA, USA. His current research interest includes machine learning and its applications to multimedia content analysis and computer vision, such as multimedia indexing and retrieval, video analysis and video semantics understanding..

Dengyin Zhang (M'17) received the B.S., M.S., and Ph.D. degrees from Nanjing University of Posts and Telecommunication, Nanjing, China, in 1986, 1989, and 2004, respectively. He is currently a Professor of the School of Internet of Things, Nanjing University of Posts and Telecommunication, Nanjing, China. He was a visiting scholar in Digital Media Lab, Umea University, Sweden, from 2007 to 2008. His research interests include image processing, networking technique, and information security.

Y. Jay Guo (F'14) received a Bachelor Degree and a Master Degree from Xidian University in 1982 and 1984, respectively, and a PhD Degree from Xian Jiaotong University in 1987, all in China. His research interest includes antennas, mm-wave and THz communications and sensing systems as well as big data technologies. He has published over 550 research papers including 280 journal papers, most of which are in IEEE Transactions, and he holds 26 patents. He is a Fellow of the Australian Academy of Engineering and Technology, a Fellow of IEEE and a Fellow of IET, and was a member of the College of Experts of Australian Research Council (ARC, 2016-2018). He has won a number of most prestigious Australian Engineering Excellence Awards (2007, 2012) and CSIRO Chairman's Medal (2007, 2012). He was named one of the most influential engineers in Australia in 2014 and 2015, respectively, and one of the top researchers in Australia in 2020.

Prof Guo is a Distinguished Professor and the Director of Global Big Data Technologies Centre (GBDTC) at the University of Technology Sydney (UTS), Australia. Prior to this appointment in 2014, he served as a Director in CSIRO for over nine years. Before joining CSIRO, he held various senior technology leadership positions in Fujitsu, Siemens and NEC in the U.K.

Prof Guo has chaired numerous international conferences and served as guest editors for a number of IEEE publications. He is the Chair of International Steering Committee, International Symposium on Antennas and Propagation (ISAP). He was the International Advisory Committee Chair of IEEE VTC2017, General Chair of ISAP2022, ISAP2015, iWAT2014 and WPMC'2014, and TPC Chair of 2010 IEEE WCNC, and 2012 and 2007 IEEE ISCIT. He served as Guest Editor of special issues on "Antennas for Satellite Communications" and "Antennas and Propagation Aspects of 60-90GHz Wireless Communications," both in IEEE Transactions on Antennas and Propagation, Special Issue on "Communications Challenges and Dynamics for Unmanned Autonomous Vehicles," IEEE Journal on Selected Areas in Communications (JSAC), and Special Issue on "5G for Mission Critical Machine Communications", IEEE Network Magazine.